Monthly Notices of the ROYAL ASTRONOMICAL SOCIETY

MNRAS **517,** 3485–3494 (2022)
Advance Access publication 2022 October 8

https://doi.org/10.1093/mnras/stac2882

Ocean dynamics and tracer transport over the south pole geysers of Enceladus

Wanying Kang ,* John Marshall, Tushar Mittal and Suyash Bire

Earth, Atmospheric and Planetary Science Department, Massachusetts Institute of Technology, Cambridge, MA 02139, USA

Accepted 2022 October 3. Received 2022 September 7; in original form 2022 May 31

ABSTRACT

Over the south pole of Enceladus, an icy moon of Saturn, geysers eject water into space in a striped pattern, making Enceladus one of the most attractive destinations in the search for extraterrestrial life. We explore the ocean dynamics and tracer/heat transport associated with geysers as a function of the assumed salinity of the ocean and various core-shell heat partitions and bottom heating patterns. We find that, even if heating is concentrated into a narrow band on the seafloor directly beneath the south pole, the warm fluid becomes quickly mixed with its surroundings due to baroclinic instability. The warming signal beneath the ice is diffuse and insufficient to prevent the geyser from freezing over. Instead, if heating is assumed to be local to the geyser (either generated in the ice due to tidal dissipation or friction or generated in the ocean as water flushes in/out of the geyser slot under tidal forcing), geyser can be sustained. In this case, the upper ocean beneath the ice becomes stably stratified creating a barrier to vertical communication, leading to transit time-scales from the core to the ice shell of hundreds of years in contrast to purported transit time-scales of weeks to months.

Key words: planets and satellites: interiors.

1 INTRODUCTION

Despite its small size (only 252 km in radius with a surface area roughly the same as Texas) and hence rapid heat loss, Enceladus retains an approximately 40 km deep global ocean beneath its ice shell (Thomas et al. 2016). Geyser-like jets are ejected into space over the south polar region (Porco et al. 2006; Howett et al. 2011; Spencer et al. 2013; Iess et al. 2014), providing a unique opportunity to peek through the ∼20 km-thick ice shell (Beuthe, Rivoldini & Trinh 2016; Hemingway & Mittal 2019) into the ocean below. Several flybys accomplished by the Cassini mission have yielded vast amounts of data, greatly improving our understanding of this small but active icy satellite. Particles and gases sampled from these jets indicate the presence of hydrogen (Waite et al. 2017), organic matter (Postberg et al. 2018), silica nanoparticles (Hsu et al. 2015), and a modestly alkaline environment (Glein, Baross & Waite 2015), all suggestive of seafloor hydrothermal activity and astrobiological potential (Waite et al. 2017; Glein, Postberg & Vance 2018; McKay et al. 2018; Taubner et al. 2018). In the planning of future missions (Tsou et al. 2012; Mora et al. 2018; MacKenzie et al. 2021), it is crucial to explore whether any nutrients or biosignatures can be transported by the ocean from the core to geyser regions, on what time-scales, and how to make best use of such information to infer the nature of the geochemical environment of the subsurface ocean. To answer these questions, we need to know not only the physical/chemical state of the ocean, but also the nature of the dynamical controls on the efficiency of tracer transport.

The ocean on icy moons is forced by salinity and heat fluxes at the ice-ocean boundary and heating at the seafloor. Just under the ice shell, the ocean temperature is close to the local freezing point of water, which is higher near the geysers where the ice is thin and the pressure is lower (see equation 11 in the supplementary material (SM)). In addition, the freezing/melting of ice will change the local salinity through brine rejection/freshwater production. There will thus be temperature and salinity gradients at the upper surface which will in turn induce ocean circulation. At the ocean bottom, hydrothermal activity powered by tidal heating in the silicate core will warm up the ocean, as described in, e.g. XX Bire et al. (2022). The magnitude of the density and hence pressure anomalies that ultimately drive circulation depend on both temperature and salinity gradients, and this dependence varies with salinity: water expands upon warming in a salty ocean but contracts upon warming in a fresh ocean. When the latter occurs (anomalous expansion), convection will not ensue until a critical temperature (∼2 K in excess of the freezing point on Enceladus) is reached. What is more, the partition of heating between the core and the ice shell determines the ocean stratification and whether convection can be triggered.

Currently, both salinity and core-shell heat partition remain poorly constrained. Observations show that both the volume of fluid emitted by the plumes and the thermal emission of the moon have strong diurnal cycles, suggesting a marked tidal modulation (Hurford et al. 2007; Hedman et al. 2013; Nimmo, Porco & Mitchell 2014; Porco, DiNino & Nimmo 2014; Hansen et al. 2017; Teolis et al. 2017). Although the combined action of faults and ice thinning can significantly amplify the tidal dissipation produced in the ice (Soucek et al. 2019), heating in the ice alone may not be enough to prevent the ocean from freezing given our current understandings in ice rheology (Beuthe 2019; Soucek et al. 2019). Use of advanced rheology models

* E-mail: wanying@mit.edu

can result in greater dissipation rates, but may still be insufficient to account for global heat loss rates (McCarthy & Cooper 2016; Renaud & Henning 2018). In addition to the volumetric tidal dissipation, it has been suggested that turbulent dissipation generated in the water as it flushes through the geyser slot (Kite & Rubin 2016) and friction along the fissures (Nimmo et al. 2007; Pleiner Sládková, Souček & Běhounková 2021) may provide additional energy to sustain the geysers. All these processes directly deposit heat to the ice, balancing the heat loss to space and cooling due to vaporization. On the other hand, significant amount of heating may be occurring in the porous silicate core through tidal dissipation (Choblet et al. 2017; Liao, Nimmo & Neufeld 2020). If core heating indeed dominates, one would expect the seafloor to be hydrothermally active, which in turn may provide the chemical gradients required to support life (Deamer & Damer 2017). However, the uncertainty associated with the core rheology is even higher, and the core needs to be in a highly deformed state in order to generate enough heat to balance loss (Rovira-Navarro et al. 2022). In the absence of direct measurements of heat production rates in the core, the ice shell and the ocean, here we consider which partitions and bottom heating patterns are most likely to sustain geysers and whether the south polar geysers can be maintained solely by heating from the silicate core alone.

Early estimates of the salinity of Enceladus' ocean are based on assumptions of thermochemical equilibrium. Considering a range of hydrothermal and freezing conditions for chondritic compositions, a salinity between 2–20 psu (g/kg) is implied (Zolotov 2007; Zolotov & Postberg 2014; Glein et al. 2018). However, at least ∼17 psu is required to keep the geysers' liquid-gas interface convectively active ensuring that they do not freeze up (Ingersoll & Nakajima 2016). Sodium-enriched samples taken by Cassini from south pole sprays have a salinity of 5–20 psu. This can be considered a lower bound since the interaction of cold water vapour sprays with their environment may lower the salinity of droplets through condensation (Postberg et al. 2009). There are uncertainties, however, since fractional crystallization and disequilibrium chemistry may partition components in such a way that geyser particles are not directly representative of the underlying ocean (Fox-Powell & Cousins 2021). Furthermore, if particles originate from a hydrothermal vent, composition can deviate far from that of the overall ocean (Choblet et al. 2017; Glein et al. 2018). Remarkably, the size of silica nanoparticles carried along in the sprays can also be used to estimate ocean salinity. Assuming an intermediate value of pH and short transport time-scale via hydrothermal vents, a salinity <40 psu is obtained (Hsu et al. 2015). In a separate line of argument, oceans with too much or too little salt may have a strong ice pump effect, leading to the erosion of ice thickness gradients. Such considerations suggest that Enceladus' ocean may have an intermediate salinity.

In this study, we will explore the plume dynamics and tracer transport under various ocean salinities, core-shell heat partitions and bottom heating patterns and investigate (1) whether geysers can be sustained solely by heating released from hydrothermal vents (Section 3.1), and (2) the time it takes for tracers to travel from the seafloor upward to the geyser (Section 3.2).

2 METHODS

To study the small-scale ocean dynamics and transport time-scales associated with geysers on Enceladus, we use the state-of-the-art Massachusetts Institute of Technology OGCM (MITgcm) (Marshall et al. 1997; MITgcm-group 2010) to simulate the 3D ocean dynamics near one geyser stripe at 100-m resolution. In an advance on previous studies (Soderlund 2019), here we account for the two-way coupling between the ice shell and ocean by allowing heat exchange between ocean and ice, resulting in freezing/melting of ice with its concomitant heat/salt flux. This, in turn, drives ocean dynamics. The geyser stripe is prescribed at the center of the domain along $y = 0$ ($-L_y/2 \leq y \leq Ly/2$, $L_y = 32$ km) as a 6.5-km Gaussian-shaped indentation on the underside of the 7-km (H_0) ice shell, with no variation in x. This ice thickness, H, does not evolve to any significant extent on the time-scales considered here. Because the ice shell is thinner near the geyser, heat is conducted through the ice more easily (see equation 6 in the SM, heat loss induced by vaporization is ignored for simplicity). Meanwhile, heat production is also stronger near the geyser due to the enhanced volumetric tidal dissipation (Beuthe 2019; Soucek et al. 2019), friction along the fissures (Nimmo et al. 2007; Pleiner Sládková et al. 2021), and the turbulence generated by having water flushing through the geyser slot (Kite & Rubin 2016). The total heating rate near/in the ice shell is conceptually represented by multiplying a thickness-dependent factor, $(H/H_0)^{p_\alpha}$, to the assumed domain-averaged heating rate (where the heat amplification factor p_α is set to -2, see equation 7 in the SM). The water just beneath the ice is relaxed towards the local freezing point, which rises with decreasing pressure (see equation 11 in the SM). These features distinguish the geyser regions from elsewhere, driving motions and heat/salt exchanges between the two. To facilitate integration out to steady state, a two-step approach is taken. We first integrate an equivalent 2D configuration ($y \times z$) out for several hundred years. This is then used to initialize the 3D model that is integrated on for another 200 yr or so.

Due to the uncertainties associated with the ocean mean salinity (Zolotov 2007; Postberg et al. 2009; Zolotov & Postberg 2014; Ingersoll & Nakajima 2016; Choblet et al. 2017; Glein et al. 2018; Fox-Powell & Cousins 2021), the core-shell heat partitioning (Travis & Schubert 2015; Choblet et al. 2017; Hemingway & Mittal 2019), and the heating pattern at the seafloor (Choblet et al. 2017), six different scenarios are explored. In the first four, a uniform bottom heating pattern is assumed, and we explore combinations of two ocean salinities (10, 30 psu) and two core-shell heat partitions (10, 90 per cent heating in the core). Hereafter, we refer to them as Sxcy, where x is the salinity and y is the percentage of heating in the core. Heating in the ice will naturally be concentrated near the poles due to the aforementioned reasons, while the core heating could be either distributed (probably due to the high porosity) or focused (Choblet et al. 2017). When the bottom heating is strong ($c = 90$ per cent), we expect its assumed pattern to be of importance. Therefore, two additional scenarios are considered: S30c90v and S10c90v, where 'v' indicates that the heating is concentrated in a narrow vent. In these two experiments, bottom heating is confined to a narrow band (not unlike the distribution hypothesized by Choblet et al. 2017) situated directly underneath the geyser, with a peak heat flux of 10 W m^{-2}. This is likely the strongest concentrated flux that can be achieved by hydrothermal systems on Enceladus (Choblet et al. 2017). These end-member scenarios will allow us to develop basic understanding of the possible tracer transport efficiencies, while the core-heating experiments ($c = 90$ per cent) are designed to investigate whether geysers can be sustained by heat generated in the core. Specifically, experiments S30c90v and S10c90v will enable us to test whether or not a bottom-concentrated heating can be transmitted to the ice without being mixed away, as is the case for plume simulations for Europa (Goodman et al. 2004; Goodman & Lenferink 2012), keeping the geyser open. Snapshots of the dynamic and thermodynamic state for each scenario are presented in the SM.

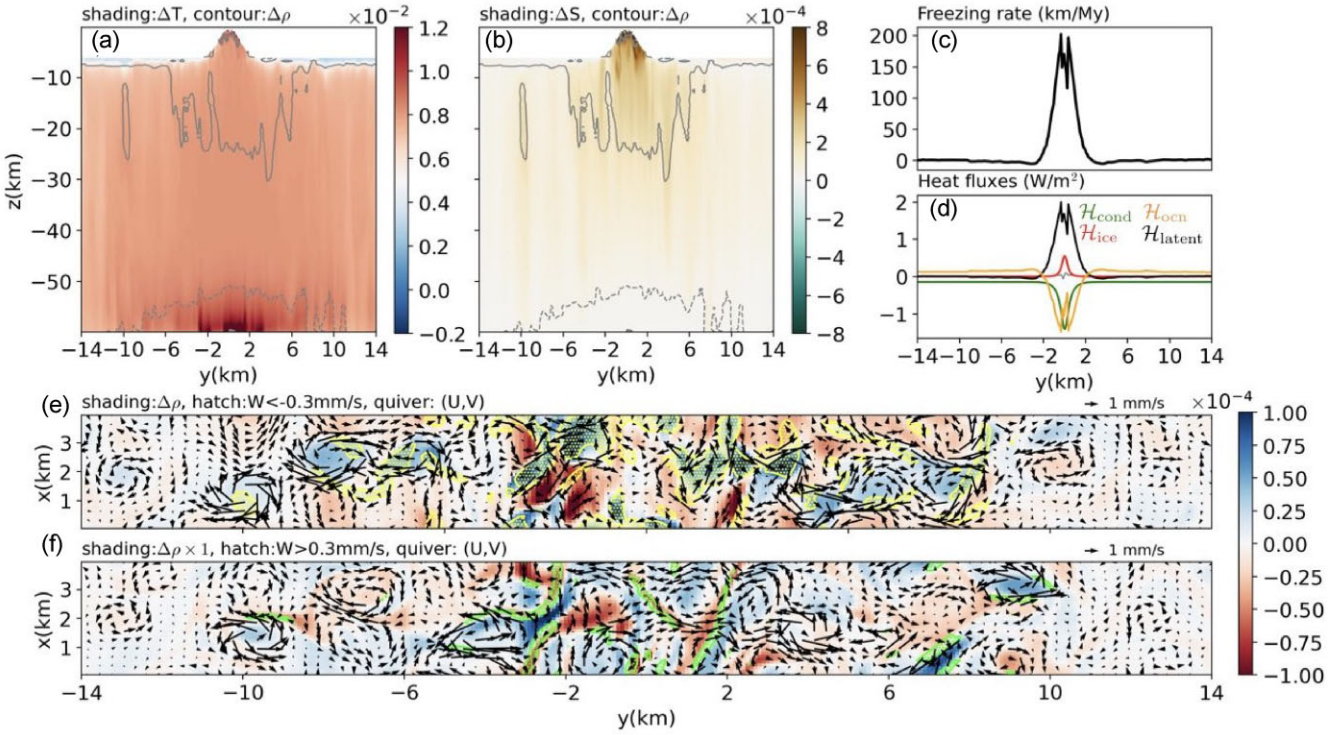

Figure 1. Snapshot taken at the end of the simulation for the S30c90v scenario, with a salinity of 30 psu with heating heavily weighted to the core. Panel (a) shows the temperature anomalies at a given x in shading and density anomalies in contours. Solid contour denote positive density anomaly and dashed contours denote negative density anomaly. From thin to thick, contours mark $\Delta\rho = \pm 10^{-4}$, $\pm 8 \times 10^{-4}$ kg m^{-3}, $\pm 5 \times 10^{-3}$ kg m^{-3}, $\pm 5 \times 10^{-2}$ kg m^{-3}. Panel (b) is similar to panel (a) except salinity is shown in place of temperature. Panels (c, d) show the freezing/melting rate and heat budget of the ice shell, respectively. In panel (d), red, orange, green, and black curves, respectively, represent the ice dissipation $\mathcal{H}_{ice}$, the heat absorbed from the ocean $\mathcal{H}_{ocn}$, the conductive heat loss through the ice $\mathcal{H}_{cond}$ and the latent heat release $\mathcal{H}_{latent}$. The grey dashed curve shows the residue of the heat budget, which should be close to zero. Panels (e, f) show the dynamics in a horizontal plane, horizontal flow speeds in quivers, density anomaly in the shading, and areas with vertical speed beyond a certain threshold (see text just above the figure) are marked by hatches. Green hatches denote upward motions and yellow hatches denote downward motions. The plane shown by panel (e) is taken just below the ice shell ($z = -9$ km), and the plane shown by panel (f) is just above the seafloor ($z = -56$ km).

3 RESULTS

3.1 Conditions required to sustain the geyser

In order to keep the geyser open, heat needs to be concentrated towards it to compensate for strong conductive heat loss (equation 6 in the SM). This is true irrespective of whether the heat source is in the ice shell or the core. If the core is the primary heat source, the ocean must carry that heat to the ice shell without significant dilution. In a salty ocean, bottom heating increases the buoyancy of water ($\alpha > 0$), which may trigger convective plumes that penetrate the entire ocean depth and deliver heat to the geysers. To test this scenario, we prescribe the bottom heating to be perfectly aligned with the geyser atop. As can be seen from Fig. 1, rather than remaining concentrated, the convective plumes become turbulent shortly after departing from the seafloor. By the time they have reached upward 10 km or so, turbulence begins to fill the entire domain as lateral instabilities spread the temperature signal horizontally leading to significant dilution.

The turbulence stems from baroclinic instability along the front that separates the warm plume water from the cold environment. Convection is always susceptible to baroclinic instability when the buoyancy source that triggers it is localized in space, as here. The phenomenon has been well documented in laboratory and theoretical studies (Saunders 1973; Jones & Marshall 1993; Maxworthy & Narimousa 1994; Legg, Jones & Visbeck 1996; Visbeck, Marshall & Jones 1996; Jacobs & Ivey 1998, 1999; Bush & Woods 1999; Okada, Ikeda & Minobe 2004). It has been found that, when the domain is deep enough for instability to take place, a line plume tends to break into a chain of horizontal vortices with a diameter of

$$L_f \sim 11(B_L/f^3)^{1/3}, \tag{1}$$

where $B_L = \int_{-L_y/2}^{L_y/2} B_A \, dy$ is the buoyancy flux per length (Bush & Woods 1999), $B_A = \alpha g Q_A/(\rho C_p)$ is the buoyancy flux per area, g is gravity, $\alpha = 4 \times 10^{-5}$/K is the thermal expansion coefficient near the bottom, Q_A is the heat flux per area, and f is the Coriolis parameter. This criterion guarantee that the circumference of the plume is sufficiently large, and the traveltime across the domain depth sufficiently slow, for instability to grow. Substituting parameters from our simulation yields a vortex diameter of $L_f \sim 200$ m, suggesting that instability will occur if the plume length is greater than 400 m. This condition is well satisfied here since the seafloor vent is assumed to have the same shape as the 'tiger stripe' seen at the surface, which is hundreds of kilometers in length. In the presence of such an instability, the heat flux will be spread out and diluted before it can affect the ice shell above. As seen in Fig. 1(f), the plume indeed splits up into vortices and turbulence. As a result, the heated water is spread over a much wider area than that of the initial source, which has a Gaussian distribution with a standard deviation of $\sigma_{core} = 200$ m (Fig. 1a). The diameter of the vortices observed in the simulation is around 1–2 km, which is five times greater than that predicted by

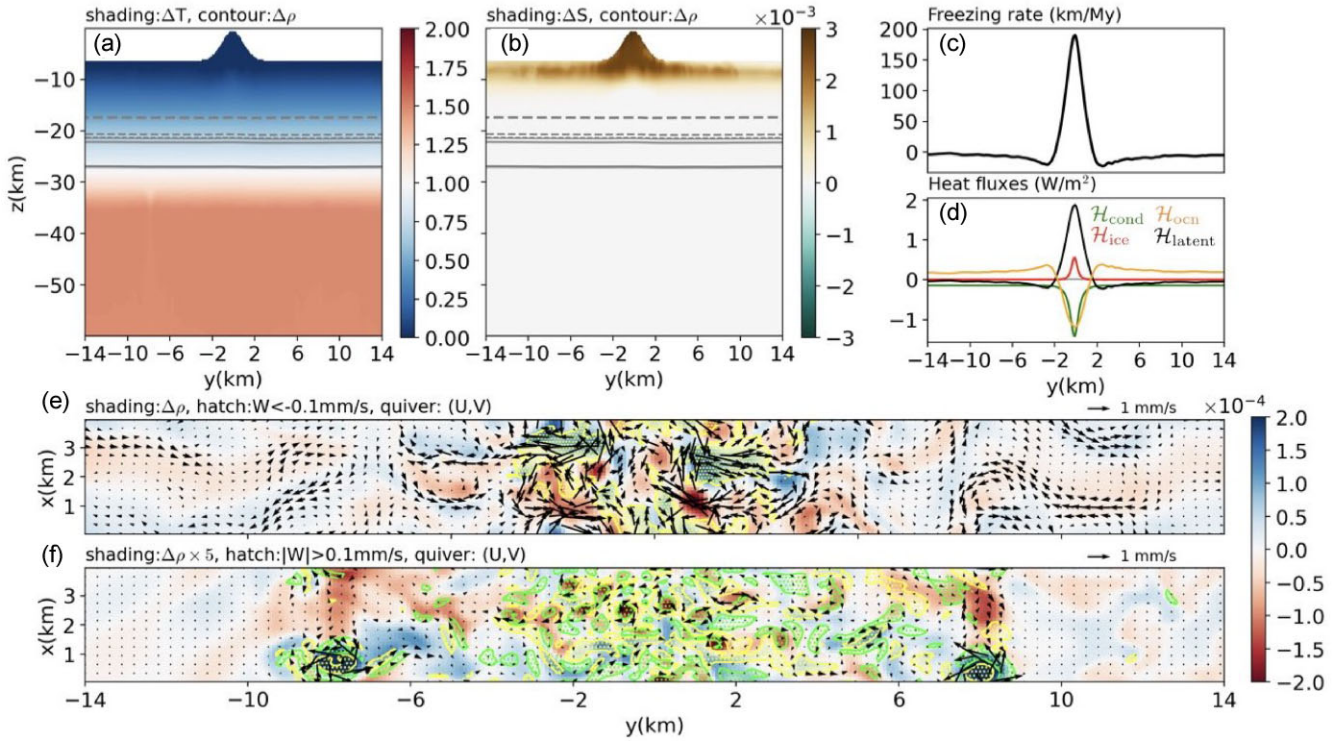

Figure 2. Same as Fig. 1 except for S10c90v, corresponding to a salinity of 10 psu with heating heavily weighted to the core.

the above scaling law. This difference may be due to the relatively large viscosity (0.05 $m^2\ s^{-1}$) employed in our numerical simulations that suppresses the instability on shorter time-scales. The vortices obtained are just small enough to fit into the 4 km wide domain. If the domain width is cut by half, only one wavelength is allowed and the flow remains laminar (see fig. S7a in the SM): when we double the domain size to the default, wavenumber-2 pattern shows up (fig. S7b in the SM), later evolving into turbulence (Fig. 1f).

Our results suggest that even if the entire ocean is convectively unstable on Enceladus, plumes and the heat carried by them from the seafloor, will be mixed away before they reach the ice shell atop assuming plausible heating rates. Since observations suggest that heat loss is highly amplified near the geyser (Spencer et al. 2006, 2013, 2018; Howett et al. 2011), heating within the ice shell close to the geyser is likely the main process preventing the geyser from freezing over (Nimmo et al. 2007; Kite & Rubin 2016; Soucek et al. 2019; Pleiner Sládková et al. 2021). This should be contrasted with studies of plume dynamics on Europa (Goodman et al. 2004; Goodman & Lenferink 2012), a much larger icy satellite. The gravity on Europa is over 10 times larger than that on Enceladus, making the buoyancy flux 10 times as strong for the same heat flux and thermal expansion coefficient.[1] As shown in Goodman et al. (2004) and Goodman & Lenferink (2012), plumes on Europa may be able to reach the surface before they experience the instability, and so the heat flux remains focused. In contrast, on Enceladus, due to its much smaller size and hence much weaker gravity, the buoyancy flux is likely to be significantly weaker. As a result, baroclinic instability is more prevalent, mixing away the plumes before they can deliver their heat flux in concentrated form to the ice.

[1]The thermal expansion coefficient α_T is likely larger on Europa due to the higher seafloor pressure and higher salinity (Hand & Chyba 2007).

Enceladus may have a rather fresh ocean with salinity lower than 22 psu (Zolotov 2007; Zolotov & Postberg 2014; Glein et al. 2018). If this is the case, fresh water contracts upon warming from below when it is near the freezing point and convection is suppressed and the warmed fluid remains confined to the bottom creating a stably stratified layer. In the presence of such a stably stratified layer (see Fig. 2a), any concentration of heat flux associated with bottom vents is again likely to be homogenized before reaching the ice shell. It should be noted that in the lowest part of the ocean, where high temperatures and pressures no longer suppress anomalous expansion, convective plumes are present and shoot upwards before breaking up, just as seen in experiment S30c90v (Fig. 2f). However, these plumes cannot penetrate into the strongly stratified layer above. In the stratified layer heat is uniformly diffused upward. Due to the low ocean salinity, the thermal expansion coefficient near the seafloor is 1–2 orders of magnitude smaller than the high salinity scenario and decays further with height. As a result, R_d is perhaps 2–3 times smaller, as reflected in the rather small plume size seen in the experiment.

Thus, whether or not the ocean is salty or fresh, we expect heat to be rather evenly delivered to the ice shell even if the source is concentrated at the bottom. As a consequence, the region of the geyser inevitably freezes because heat loss there occurs at a greater rate than elsewhere (Figs 1c and 2c). Through brine rejection, freezing makes the water salty and thus dense (Figs 1b and 2b), triggering convection from the top. The associated buoyancy flux per length B_L can be estimated thus: $\int_{-\sigma_H}^{\sigma_H} \beta g q S_0\ dy \approx 2\sigma_H \beta g \bar{q} S_0 \approx 2 \times 10^{-8}\ m^3\ s^{-3}$. This is comparable to the buoyancy flux induced by hydrothermal heating at the bottom. Here, q is the freezing rate, $\bar{q} \sim 100\ km\ My^{-1}$ near the geyser, $\sigma_H = 1$ km is the width of the geyser and β is the haline contraction coefficient at mean salinity S_0. This explains why the size of the salinity-driven vortex near the top is similar to that of the heat-driven vortex near the bottom – Fig. 1(h). As the downward

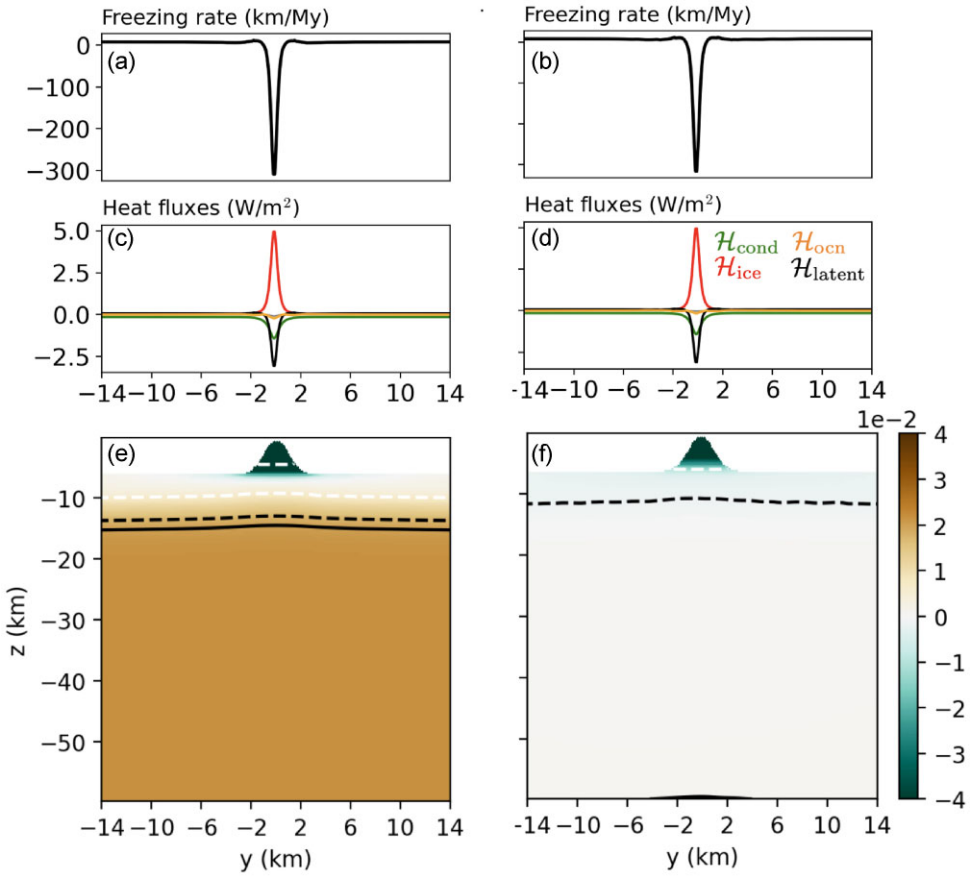

Figure 3. Heat budget and ocean circulation in the shell-heating scenarios. Panels (a, b) show the freezing rate (left *y*-axis, black solid) and panels (c, d) show the heat budget terms (right *y*-axis, dashed curves) of the ice shell for S30c10 and S10c10, respectively. Panels (e, f) show salinity anomalies by shading and density anomalies by contours. The solid contour denotes a positive density anomaly, negative denotes a negative density anomaly. The black curves mark $\pm 10^{-3}$ kg m^{-3}, and white curves $\pm 10^{-2}$ kg m^{-3}.

convective plumes breakup, turbulence is generated, spreading the salty water into the surroundings (Fig. 1b), while mixing the warm water near the geyser with the cold water under the thicker ice shell on the periphery (see Figs 1a and 2a). As a result, heat is transported away from the geyser area, as quantified by the ice shell heat budget (see orange curve in Figs 1d and 2d). This almost doubles the geyser's freezing rate triggered by the initial conductive heat loss (green curve).

To summarize, irrespective of the assumed ocean salinity, concentrated heating from the bottom is unlikely to remain concentrated by the time it reaches the ice shell, leading inevitably to the freezing over of the geyser. When bottom heating is not localized (S30c90 and S10c90), the freezing rate and heat budgets are remarkably similar to that obtained when it is concentrated (S30c90v and S10c90v), indicating that the bottom heating pattern is 'forgotten' as it is transmitted upward.

Given the difficulty in sustaining geysers in the core-heating scenarios, we now consider the case in which tidal heating is assumed to occur in the ice shell itself. The volumetric tidal heating rate is expected to be highly concentrated near the faults (Soucek et al. 2019). In addition, friction along fissures (Nimmo et al. 2007; Pleiner Sládková et al. 2021) and turbulence induced by water flow through the opening geyser (Kite & Rubin 2016) will further enhance the heat production near the geyser. A total heat production rate indirectly proportional to the ice thickness H to the second power ($p_\alpha = -2$) is sufficient to balance the ocean heat transport away from the geyser and the conductive loss rate that is inversely proportional to H, as shown by Figs 3(a) and (b).

3.2 Plume dynamics and tracer transport time-scales

Future sensors are likely to be deployed above the ice, and so it is important to come to some understanding of likely bottom-to-top transport time-scales. Such understanding will inform us of how long chemical components, introduced near the seafloor (Parkinson et al. 2008; Glein et al. 2015; McKay et al. 2018), have time to react with the ocean before reaching the underside of the ice before being ejected out in a geyser. To approach this question, we release two types of passive tracer: one which is uniform in space at the seafloor and the other which is localized in space, at $y = 0$, right under the geyser. The concentration of the tracer is restored to 1 at the bottom of the model, mimicking a chemical/biological process that keeps the tracer concentration at a certain level. After 20–200 yr, the tracer distributions found in the six scenarios are shown in Fig. 4. As we now discuss, the tracer transport time-scale is typically in excess of hundreds of years, but can vary significantly depending on the assumed ocean salinity and core-shell heat partition.

Tracer transport is governed by ocean dynamics that responds to both the prescribed bottom heating and the salinity flux associated with freezing/melting of the ice above. Strong bottom heating (as in

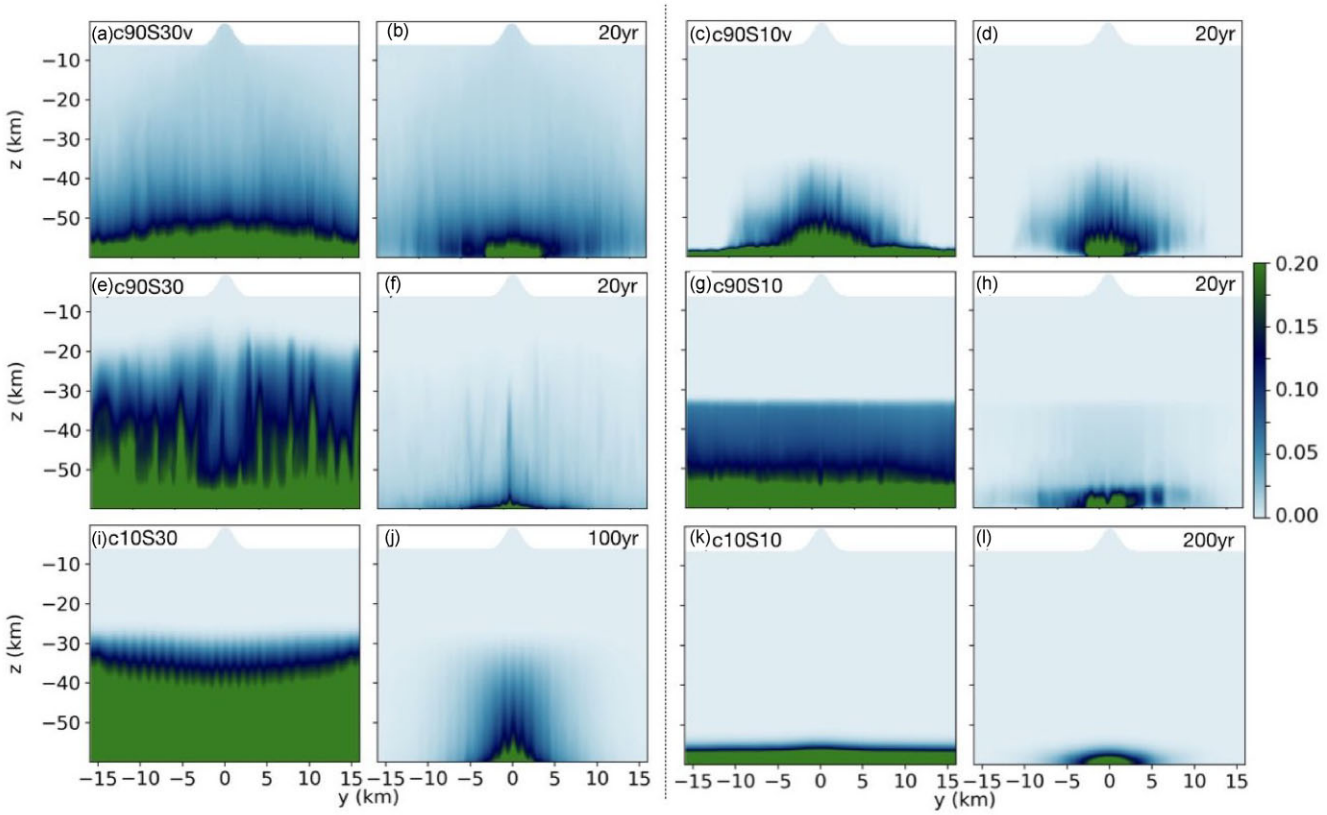

Figure 4. Tracer distribution at the end of our simulations. Tracers are released uniformly from the entire seafloor in panels (a, c, e, g, i, k), but only from a narrow zone on the seafloor right under the geyser in panels (b, d, f, h, j, l). The left two columns, from top to bottom are results for S30c90v, S30c90, S30c10. The right two columns, from top to bottom are for S10c90v, S10c90, S10c10. The length of integration time since tracers release are marked on the right for each scenario.

S30c90, S30c90v, S10c90, S10c90v) is expected to trigger stronger convection and hence more efficient transport compared to those with weak bottom heating (S30c10, S10c10). Furthermore, ocean salinity determines the sign and the magnitude of the thermal expansion coefficient. The same bottom heating will induce much weaker convection, if at all, in a fresh ocean due to the anomalous expansion of water near the freezing point. Thus very general considerations suggest that S30c90v and S30c90 should facilitate the most efficient tracer transport.

3.2.1 Core-heating + salty ocean (S30c90v and S30c90)

The tracer concentrations after 20 yr of integration are presented in Figs 4(a) and (e) for the two core-heating and salty-ocean scenarios. Even in these optimal scenarios, tracers have only been transported 10 km or so above the seafloor after 20 yr. The tracer transport efficiency varies with the horizontal distance from the geyser (S30c90v and S30c90), indicating that the very short transport time-scale (a month) suggested by Hsu et al. (2015) may be hard to achieve without extra buoyancy provided by, for example, gas bubbles.

In the localized heat source experiment, S30c90v, one would expect the tracer transport to only occur near $y = 0$, where the heat source is located. However, as discussed above, baroclinic eddies grow along the edge of the heating line due to the temperature contrast between the hot plume and the cold ambient water (Saunders 1973; Visbeck et al. 1996; Legg et al. 1996; Jacobs & Ivey 1999, 1998). These eddies induce geostrophic turbulence and facilitate strong lateral mixing, leading to the almost uniform vertical tracer transport seen in Fig. 4(a). In a turbulent flow, tracer transport time-scale cannot be estimated by dividing the total distance over plume speed, as in Choblet et al. (2017), because tracers undergo many ups and downs before reaching the surface, switching from one convective element to the next. The resultant transport time-scale obtained here is at least hundreds of years, thousands of times longer than argued by Choblet et al. (2017).

In contrast, in the presence of homogeneous bottom heating as in S30c90, there is no externally forced temperature gradient supporting baroclinic instability. Instead, the convective plumes become organized into cones, surrounded by an azimuthal 'rim current'. This phenomenon has been well-studied experimentally and numerically (Jones & Marshall 1993; Goodman et al. 2004). The scale over which the plumes congregate is given by the 'cone scaling'

$$l_{\text{cone}} = 1.4 D^{1/2} \left(B_A / f^3 \right)^{1/4}, \tag{2}$$

where D is the depth of the domain. The configuration of S30c90 yields a cone size of $l_{\text{cone}} = 300$ m, which is broadly consistent with the scales seen in Fig. 5(a). Moreover, fingerprints of the clustering of the convectively modified fluid in to cones can be seen in the tracer distribution of Fig. 4(e).

Of the six scenarios considered here, only S30c90v and S30c90 are convectively unstable under the geyser due to the influence of salinity effects, as shown by the density contours in Fig. 1(b) and fig. A5b. The

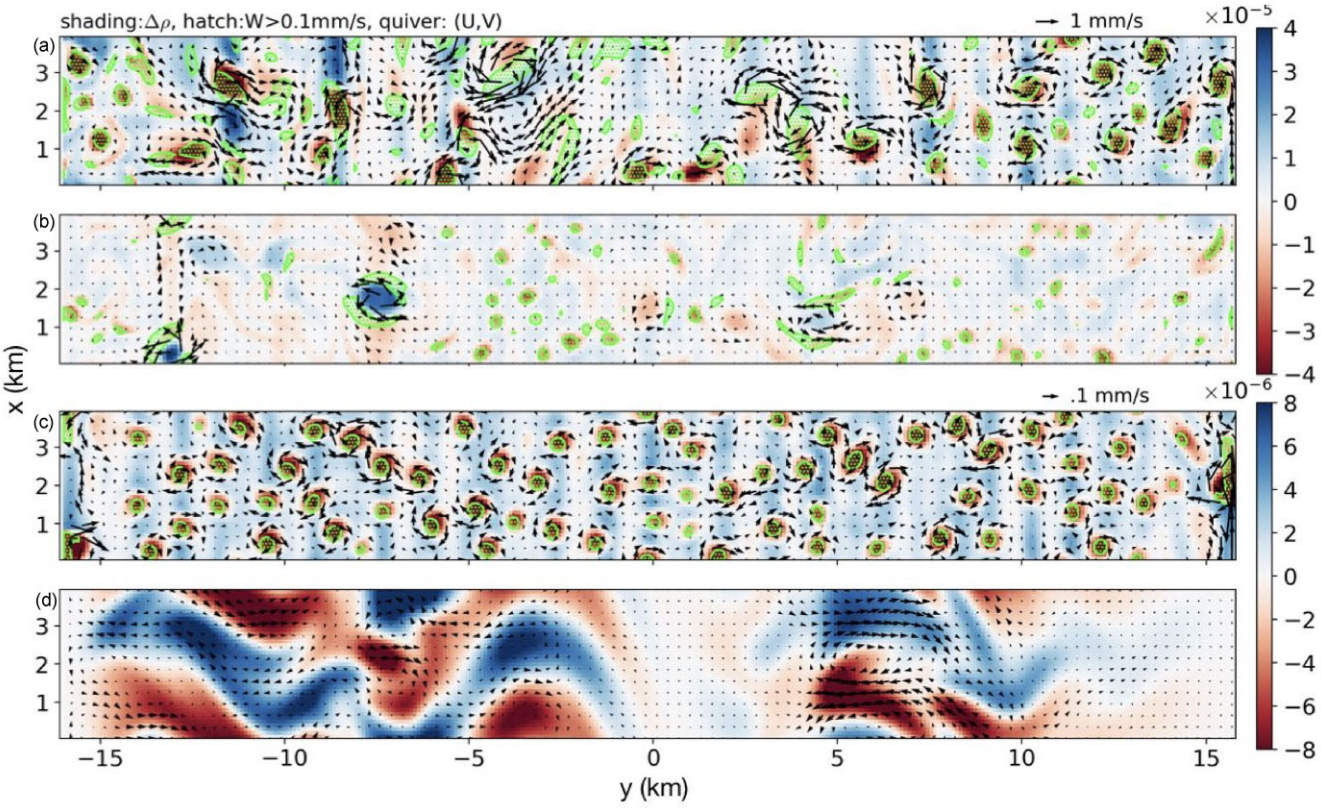

Figure 5. Ocean dynamics close to the bottom for the uniform bottom heating scenarios and the shell heating scenarios. These plots are the same as the panel (e) of Fig. 1. From top to bottom we present cases S30c90, S10c90, S30c10, and S10c10.

lower part of the ocean convects upward driven by the bottom heating whilst, at the same time, the upper ocean convects downward forced by the salinity flux associated with the freezing of the geyser (Fig. 1c and fig. A5f). In S30c90, the upward tracer transport by thermal convection seems to be inhibited in the vicinity of the geyser due to downward, salinity-driven convection quenching it from above. Instead, in S30c90v, tracer transport is almost uniform due to strong lateral mixing by turbulence generated through baroclinic instability (Section 3.1).

3.2.2 *Core-heating + fresh ocean (S10c90 and S10c90v)*

In a fresh ocean, the near bottom dynamics remain qualitatively similar to the high salinity case, but become less active (see Fig. 2f and fig. A3i). This is because the same heat flux now induces a weaker buoyancy flux due to the much lower thermal expansion coefficient. The less vigorous dynamics is not only manifested by a weaker density gradient and a weaker 'rim current', but also scales are reduced by a factor of 2–3. According to equations (1) and (2), broadly consistent with a 30 fold reduction of α (the mean α of the convective layer is 3×10^{-5}/K in experiment S30c90 and 1×10^{-6}/K in S10c90).

An interesting phenomenon observed in the fresh case is that, along with the upward-directed turbulent plumes, there are well-organized cold plumes shooting downwards, whose size is even larger than the upwelling convection (see Fig. 2f). The same phenomenon is also seen in the uniform bottom heating case (Fig. 5b). Irrespective of whether bottom heating is concentrated, in equilibrium the net upward heat flux must be the same at all levels. In other words, the upper surface must cool at the same rate as the bottom is warmed, and so upward and downward convective plumes should, in the net, be in balance with one-another. However, in our simulations, the downwelling plumes appear to be much larger and stronger. This asymmetry may be related to the strong temperature gradient in the upper part of the ocean and the depression of anomalous expansion with pressure. Near the upper boundary of the convective layer ($z = -34$ km), the perturbation associated with convective turbulence creates, for example, a cold bubble which sinks into the convective layer. The deeper it gets, the greater is the pressure leading to a more positive α and hence faster downward acceleration. As a result, this cold bubble sinks with increasing acceleration until striking the bottom. In contrast, the temperature gradient near the seafloor is weak and convective plumes shooting upward will be weakened by the decrease of α, and eventually suppressed once α becomes negative.

The ocean is stably stratified and diffusive in its upper regions. This stratified layer is a consequence of the anomalous expansion of fresh water. Forced by strong bottom heating, temperature increases approaching the seafloor (Fig. 2a and fig. A4a). However, such a temperature gradient stabilizes the upper part of the ocean, because fresh water contracts upon warming ($\alpha < 0$) at low pressure near the freezing point. As pressure increases with depth, the temperature range over which α is negative gradually shrinks, and eventually vanishes around $z = -30$ km (the critical level). Only below this level does water expands upon warming allowing convective plumes to be triggered (Fig. 2f and 5c). Transporting tracers across the stratified layer may be a challenge due to the sluggish dynamics. This is reflected by the very low tracer concentrations observed above the critical level. If transport only occurs through vertical diffusion, and

assuming a vertical diffusivity of 0.001 $m^2\ s^{-1}$, 10 kyr is needed to diffuse through a 20 km layer.[2]

3.2.3 Shell heating

When the heating is primarily in the ice shell, the dynamics in the lower part of the ocean becomes even weaker. As shown in Fig. 5(c), the combination of shell heating and a salty ocean (S30c10) facilitates the same columnar dynamics as S30c90, with buoyant fluid convecting upward under rotational control. Since the bottom heat flux here is nine times smaller than S30c90, the plume size is about half as large, as can be seen by comparing Fig. 5(c) with Fig. 5(a). By yr-20, tracers are only advected some 10 km above the seafloor (see fig. A2e), and by yr-100, they have only reached 30 km, half-way across the depth of the ocean (Fig. 4i).

If, by contrast, the ocean is fresh (S10c10), the entire ocean is stably stratified (Fig. 3f). Unlike in S90c10, there is no convective layer near the bottom (Fig. 5d) because the top-to-bottom temperature gradient required to conduct the weak bottom heating away (18.7 mW m^{-2}) is only 0.2 K (assuming $\kappa_v = 10^{-3}\ m^2\ s^{-1}$), not enough to make the bottom α positive despite the high pressure there. In the absence of convection, vertical tracer transport is almost negligible. By the end of 200 yr of integration, the tracers have only travelled 4 km (see Fig. 4 kl), broadly consistent with a diffusion time-scale.

In the upper part of the ocean, both of our shell-heating scenarios have a stably stratified layer, because the fresh water produced by ice melting near the geyser fills up the indentation beneath the geyser and diffuses downward, forming a freshwater lens. Again, this stratified layer may extend the tracer transport time-scale to thousands of years, if vertical diffusion is the only process facilitating transport. Finally, we note that the stratified layer is not completely quiescent. Horizontal density gradients induced by the inhomogeneous melting trigger gravity waves, as can be seen in figs S1h and S2h.

To conclude, none of our six scenarios transports a significant amount of tracer to the geyser by the end of the simulations. Even with the help of convective plumes powered by strong bottom heating (S30c90, S30c90v), tracers are still 10–20 km away from the geyser by yr 20. Tracer transport is even slower when bottom heating is weaker and/or ocean salinity is low. S30c10 transports tracers 10–20 km above the seafloor by yr-100. In S10c90, since the upper part of the ocean is strongly stratified, the tracer transport is halted half-way and is unlikely to reach further. In S10c10, the tracers almost completely dwell at the seafloor because the ocean is stratified and quiescent.

In our S30c90v and S10c90v experiments, we also released a second type of tracer which is only produced at $y = 0$, right under the geyser where the bottom heat flux is concentrated. As shown in Figs 4(a–d), near $y = 0$ the concentration of this second tracer is comparable to that of the first, indicating that the tracer that reaches the geyser may be mostly from the vent area – the tracer transport time-scale does not change significantly if the tracer is only produced near the vent. As a reference, this initially concentrated tracer is carried out in all our experiments.

4 DISCUSSION

We have investigated how ocean dynamics and tracer/heat transport near the south polar geysers of Enceladus are affected by ocean salinity, the partition of heat between core and the shell and the heating distribution at the seafloor. Two key questions have motivated our study:

(i) What are the conditions most likely to result in the geyser being self-sustained?

We find that only when the ice shell is the predominant heat source (S10c10, S30c10), can that heat be focused near the geyser, preventing it from freezing up. If the heat source is primarily the core, even if it is perfectly aligned with the geyser (as in S30c90v and S10c90v), convective plumes become baroclinically unstable, leaking most of the heat away from the geyser regions before reaching the ice. As a result, the geyser will freeze and close up.

(ii) How long does it take for tracers to be transported from the seafloor to the geyser region?

Scenarios in which bottom-induced convection occurs over the entire ocean (S30c90, S30c90v) may be able to transport a significant amount of tracer to the geyser within a 100 yr or so. Other scenarios either cannot transport tracer at all (S10c10) or the transport only reaches half-way (S10c90, S10c90v, S30c10) due to the stratification in the upper part of the ocean. Diffusion is the only process that can transport tracers across the stratified layer, but only on time-scales of hundreds of years.

Given that a bottom-concentrated heat flux is diluted as it is carried through the ocean, active polar geysers are likely driven by heating in the ice/ocean occurring close to the geyser. Since the total heat loss through the geyser by far dominates other regions (Howett et al. 2011; Spencer & Nimmo 2013; Spencer et al. 2018), either tidal dissipation in the ice (Soucek et al. 2019) or turbulent dissipation in the water caused by the tide-driven flow through the geyser slots (Kite & Rubin 2016) is the primary heat source. Therefore, among all the scenarios considered here, S10c10 and S30c10 are likely the most relevant. These suggest that tracer transport time-scales are many hundreds of years. This is far greater than the month-to-year transport time-scale suggested by Hsu et al. (2015), and broadly aligns with the $\gg$100 yr estimate given by Zeng & Jansen (2021). If this is the case then, when interpreting the chemical composition of ejecta, one must account for the reaction of possible biosignatures emanating from the bottom with the ocean on their way up to the surface.

There are important caveats that should be noted. First, we have ignored the impact of erupting plumes upon the ocean. Based on the measurements of the Ultraviolet Imaging Spectrometer (Hansen et al. 2011), the vapour production rate is estimated to be total around 200 $kg\ s^{-1}$. Such eruptions have three major impacts: they drive flow towards the geyser to fill up the vacuum, extra heat is required to sustain the vaporization, and local salinity is increased because salt is left behind. However, we expect the impact of eruptions is likely small. The flow speed required to compensate a mass sink of 200 $kg\ s^{-1}$ over a total length of ~420 km[3] is only 0.04 mm s^{-1}, far weaker than the dynamics found here, even if the mass convergence is constrained to the top 10 m of the ocean. The heat required to sustain 200 $kg\ s^{-1}$ of vaporization is 0.5 GW or 15 mW m^{-2} averaged over an area of 180 km × 180 km, small compared to the heat loss rate here (equation 6 in the SM). However, as pointed out by Nimmo et al. (2007), more vapour could evaporate from the ocean and re-condense on the surface of the ice shell, warming the surface. The resultant heat loss may be comparable or stronger

[2]The diffusive time-scale is $\tau_{\rm diff} = H^2/\kappa_v$, where $\kappa_v = 0.001\ m^2\ s^{-1}$ is the vertical diffusivity and H is the vertical scale.

[3]Each geyser is around 130 km long and there are four of them (Porco et al. 2006).

than the conductive heat loss. The associated salinity flux is only equivalent to freezing at a rate of 4 km My^{-1} over a 3-km wide geyser. This is again far smaller than the freezing/melting rate found in our simulations.

Secondly, it should be noted that the representation of the heat production in/near the ice shell ($\mathcal{H}_{ice}$, equation 7 in the SM) and the heat loss rate ($\mathcal{H}_{cond}$, equation 6 in the SM) are both highly idealized, and so quantitative results, such as the freezing/melting rate in each scenario, are only broad estimates. The heat production rate used here is assumed to be inversely proportional to the ice thickness H square (equation 7 in the SM). However, the heating generated near/in the ice shell, by construction only plays a minimal role in the core-heating experiments ($c = 90$ per cent)n, and thus the assumed heating profile should not affect our conclusions #1. The heat loss rate is assumed to be inversely proportional to the ice thickness H based on the behaviour of heat conduction. However, as mentioned above, vaporization may significantly enhance the heat loss rate near the geyser, further accelerating the freezing of the geyser in the core-heating scenarios. In fact, the extent to which heat is concentrated will not make a qualitative difference, as long as it amplifies near the geysers, as observed (Howett et al. 2011; Spencer et al. 2013, 2018). For the shell-heating scenarios ($c = 10$ per cent), however, the relative strength of the geyser heat production with respect to that of the heat loss due to conduction and vaporization is key to the sustainability of the geyser. Previous tidal dissipation calculations which consider the impact of faults suggests that heat generation should be highly concentrated near the geyser, likely more concentrated than assumed here Soucek et al. (2019). Furthermore, the friction along the fissures (Nimmo et al. 2007; Pleiner Sládková et al. 2021) and the turbulence generated by flushing water through the open slot (Kite & Rubin 2016) produces additional heat near the geysers. Whether these processes can sustain the observed heat loss rate from the south polar terrain is beyond the scope of this study.

Thirdly, we have ignored the thermodynamic and dynamic interactions between the south pole and the rest of the ocean and assume that the heat budget is local. In reality, the south polar ocean is fully connected with the broader ocean. Forced by inhomogeneous heat and salinity fluxes from the ice, a meridional circulation could form that transports heat equatorward. This equatorward heat convergence cannot exceed the conductive heat loss rate through the equatorial ice shell. Observations tell us that the heat flux passing through the geysers completely dominates the heat flux anywhere (Porco et al. 2006; Howett et al. 2011; Spencer et al. 2013, 2018). This suggests that the heat budget over the south pole of Enceladus may be roughly in balance. That said, future studies should explore the role of localized geysers in the general circulation. Finally, given that Enceladus' core is likely to be porous, water may be allowed to penetrate the core-water boundary (Choblet et al. 2017). This is not accounted in this study and could enhance the tracer transport.

ACKNOWLEDGEMENTS

This work was carried out in the Department of Earth, Atmospheric and Planetary Science (EAPS) in MIT. WK acknowledges endowed funds in EAPS. JM and SB acknowledge part-support from NASA Astrobiology Grant 80NSSC19K1427 'Exploring Ocean Worlds'. We all thank 'Exploring Ocean Worlds' for helpful support and discussions, and Prof. Edwin Kite for helpful suggestions/comments.

DATA AVAILABILITY

The supporting information provides detailed description of our model set-up. We would like to provide more code and data upon reasonable request.

REFERENCES

Beuthe M., 2019, Icarus, 332, 66
Beuthe M., Rivoldini A., Trinh A., 2016, Geophys. Res. Lett., 43, 10,088
Bire S., Kang W., Ramadhan A., Campin J.-M., Marshall J., 2022, J. Geophys. Res.: Planets, 127, e2021JE007025
Bush J. W., Woods A. W., 1999, J. Fluid Mech., 388, 289
Choblet G., Tobie G., Sotin C., Běhounková M., Čadek O., Postberg F., Souček O., 2017, Nat. Astron., 1, 841
Deamer D., Damer B., 2017, Astrobiology, 17, 834
Fox-Powell M. G., Cousins C. R., 2021, J. Geophys. Res.: Planets, 126, e2020JE006628
Glein C. R., Baross J. A., Waite J. H., Jr, 2015, Geochim. Cosmochim. Acta, 162, 202
Glein C., Postberg F., Vance S., 2018, in Schenk M. P., Clark R. N., Howett C. J. A., Verbiscer A. J., Waite J. H., eds, Enceladus and the Icy Moons of Saturn. University of Arizona Press, Tucson, p. 39
Goodman J. C., Collins G. C., Marshall J., Pierrehumbert R. T., 2004, J. Geophys. Res., 109, E03008
Goodman J. C., Lenferink E., 2012, Icarus, 221, 970
Hand K., Chyba C., 2007, Icarus, 189, 424
Hansen C. et al., 2011, Geophys. Res. Lett., 38, L11202
Hansen C., Esposito L., Aye K.-M., Colwell J., Hendrix A., Portyankina G., Shemansky D., 2017, Geophys. Res. Lett., 44, 672
Hedman M. et al., 2013, Nature, 500, 182
Hemingway D. J., Mittal T., 2019, Icarus, 332, 111
Howett C. J. A., Spencer J. R., Pearl J., Segura M., 2011, J. Geophys. Res.: Atmos., 116, 189
Hsu H.-W. et al., 2015, Nature, 519, 207
Hurford T., Helfenstein P., Hoppa G., Greenberg R., Bills B., 2007, Nature, 447, 292
Iess L. et al., 2014, Science, 344, 78
Ingersoll A. P., Nakajima M., 2016, Icarus, 272, 319
Jacobs P., Ivey G., 1998, J. Fluid Mech., 369, 23
Jacobs P., Ivey G., 1999, Dyn. Atmos. Oceans, 30, 149
Jones H., Marshall J., 1993, J. Phys. Oceanogr., 23, 1009
Kite E. S., Rubin A. M., 2016, Proc. Natl. Acad. Sci., 113, 3972
Legg S., Jones H., Visbeck M., 1996, J. Phys. Oceanogr., 26, 2251
Liao Y., Nimmo F., Neufeld J. A., 2020, J. Geophys. Res.: Planets, 125, e2019JE006209
MacKenzie S. M. et al., 2021, Planet. Sci. J., 2, 77
Marshall J., Adcroft A., Hill C., Perelman L., Heisey C., 1997, J. Geophys. Res., 102, 5,753
Maxworthy T., Narimousa S., 1994, J. Phys. Oceanogr., 24, 865
McCarthy C., Cooper R. F., 2016, Earth Planet. Sci. Lett., 443, 185
McKay C., Davila A., Glein C., Hand K., Stockton A., 2018, in Schenk P. M., Clark R. N., Howett C. J. A., Verbiscer A. J., Waite J. H., eds, Enceladus and the Icy Moons of Saturn. University of Arizona Press, Tucson, p. 437
MITgcm-group, 2010, Online documentation, MITgcm User Manual. MIT/EAPS, USA
Mora M. F., Jones S. M., Creamer J., Willis P. A., 2018, Electrophoresis, 39, 620
Nimmo F., Porco C., Mitchell C., 2014, AJ, 148, 46
Nimmo F., Spencer J., Pappalardo R., Mullen M., 2007, Nature, 447, 289
Okada N., Ikeda M., Minobe S., 2004, J. Oceanogr., 60, 927
Parkinson C. D., Liang M.-C., Yung Y. L., Kirschivnk J. L., 2008, Orig. Life Evol. Biosph., 38, 355
Pleiner Sládková K., Souček O., Běhounková M., 2021, Geophys. Res. Lett., 48, e2021GL094849
Porco C. C. et al., 2006, Science, 311, 1393
Porco C., DiNino D., Nimmo F., 2014, AJ, 148, 45

Postberg F. et al., 2018, Nature, 558, 564
Postberg F., Kempf S., Schmidt J., Brilliantov N., Beinsen A., Abel B., Buck U., Srama R., 2009, Nature, 459, 1098
Renaud J. P., Henning W. G., 2018, ApJ, 857, 98
Rovira-Navarro M., Katz R. F., Liao Y., van der Wal W., Nimmo F., 2022, J. Geophys. Res.: Planets, 127, e2021JE007117
Saunders P. M., 1973, J. Phys. Oceanogr., 3, 61
Soderlund K. M., 2019, Geophys. Res. Lett., 46, 8700
Soucek O., Behounkova M., Cadek O., Hron J., Tobie G., Choblet G., 2019, Icarus, 328, 218
Spencer J. et al., 2006, Science, 311, 1401
Spencer J. R., Howett C. J. A., Verbiscer A., Hurford T. A., Segura M., Spencer D. C., 2013, European Planetary Science Congress, 8, EPSC2013
Spencer J. R., Nimmo F., 2013, Annu. Rev. Earth Planet Sci., 41, 693
Spencer J., Nimmo F., Ingersoll A. P., Hurford T., Kite E., Rhoden A., Schmidt J., Howett C., 2018, in Schenk P. M., Clark R. N., Howett C. J. A., Verbiscer A. J., Waite J. H., eds, Enceladus and the Icy Moons of Saturn. University of Arizona Press, Tucson, p. 163
Taubner R.-S. et al., 2018, Nat. Commun., 9, 1
Teolis B. D., Perry M. E., Hansen C. J., Waite J. H., Porco C. C., Spencer J. R., Howett C. J., 2017, Astrobiology, 17, 926
Thomas P., Tajeddine R., Tiscareno M., Burns J., Joseph J., Loredo T., Helfenstein P., Porco C., 2016, Icarus, 264, 37
Travis B. J., Schubert G., 2015, Icarus, 250, 32
Tsou P. et al., 2012, Astrobiology, 12, 730
Visbeck M., Marshall J., Jones H., 1996, J. Phys. Oceanogr., 26, 1721
Waite J. H. et al., 2017, Science, 356, 155
Zeng Y., Jansen M. F., 2021, The Planetary Science Journal, 2, 151
Zolotov M. Y., 2007, Geophys. Res. Lett., 34, L23203
Zolotov M. Y., Postberg F., 2014, LPI, 2496

SUPPORTING INFORMATION

Supplementary data are available at *MNRAS* online.

Figure S1: Snapshot taken at the end of the simulation for the S10c10 scenario.
Figure S2: Similar to Fig. 1, except for the S30c10 scenario.
Figure S3: Similar to Fig. 1, except for the S10c90 scenario.
Figure S4: Similar to Fig. 1, except for the S10c90v scenario.
Figure S5: Similar to Fig. 1, except for the S30c90 scenario.
Figure S6: Similar to Fig. 1, except for the S30c90v scenario.
Figure S7: Similar to fig. 6 panel (i). Panel (a) shows results for an experiment with half-domain width, and panel (b) shows the initial stage of simulation after the domain is re-extended to the full width.
Figure S8: Bottom ocean dynamics resolved by 10-m resolution model for S30c90.
Table S1: Default model parameters.

Please note: Oxford University Press is not responsible for the content or functionality of any supporting materials supplied by the authors. Any queries (other than missing material) should be directed to the corresponding author for the article.

This paper has been typeset from a TEX/LATEX file prepared by the author.